The Astronomical Journal, 154:225 (13pp), 2017 December
https://doi.org/10.3847/1538-3881/aa906b

ALMA 1.3 mm Map of the HD 95086 System

Kate Y. L. Su[1,2], Meredith A. MacGregor[3,14], Mark Booth[4], David J. Wilner[3], Kevin Flaherty[5], A. Meredith Hughes[5],
Neil M. Phillips[6], Renu Malhotra[7], Antonio S. Hales[8,9], Sarah Morrison[7,15], Steve Ertel[1], Brenda C. Matthews[10,11],
William R. F. Dent[8], and Simon Casassus[12,13]

[1] Steward Observatory, University of Arizona, 933 N Cherry Avenue, Tucson, AZ 85721, USA
[2] Institute of Astronomy and Astrophysics, Academia Sinica, P.O. Box 23-141, Taipei 106, Taiwan
[3] Harvard-Smithsonian Center for Astrophysics, 60 Garden Street, Cambridge, MA 02138, USA
[4] Astrophysikalisches Institut und Universitätssternwarte, Friedrich-Schiller-Universität Jena, Schillergäßchen 2–3, D-07745 Jena, Germany
[5] Department of Astronomy, Van Vleck Observatory, Wesleyan University, Middletown, CT 06459, USA
[6] Joint ALMA Observatory (JAO); European Southern Observatory, Santiago, Chile
[7] Lunar and Planetary Laboratory, University of Arizona, Tucson, AZ 85721, USA
[8] Joint ALMA Observatory, Alonso de Córdova 3107, Vitacura 763-0355, Santiago, Chile
[9] National Radio Astronomy Observatory, 520 Edgemont Road, Charlottesville, VA 22903-2475, USA
[10] National Research Council of Canada Herzberg Astronomy and Astrophysics Programs, Victoria, BC, V9E 2E7, Canada
[11] University of Victoria, 3800 Finnerty Road, Victoria, BC, V8P 5C2, Canada
[12] Departamento de Astronomia, Universidad de Chile, Casilla 36-D, Santiago, Chile
[13] Millennium Nucleus "Protoplanetary Disks", Santiago, Chile

Received 2017 August 9; revised 2017 September 22; accepted 2017 September 28; published 2017 November 14

Abstract

Planets and minor bodies such as asteroids, Kuiper-Belt objects, and comets are integral components of a planetary system. Interactions among them leave clues about the formation process of a planetary system. The signature of such interactions is most prominent through observations of its debris disk at millimeter wavelengths where emission is dominated by the population of large grains that stay close to their parent bodies. Here we present ALMA 1.3 mm observations of HD 95086, a young early-type star that hosts a directly imaged giant planet b and a massive debris disk with both asteroid- and Kuiper-Belt analogs. The location of the Kuiper-Belt analog is resolved for the first time. The system can be depicted as a broad ($\Delta R/R \sim 0.84$), inclined ($30° \pm 3°$) ring with millimeter emission peaked at 200 ± 6 au from the star. The 1.3 mm disk emission is consistent with a broad disk with sharp boundaries from 106 ± 6 to 320 ± 20 au with a surface density distribution described by a power law with an index of -0.5 ± 0.2. Our deep ALMA map also reveals a bright source located near the edge of the ring, whose brightness at 1.3 mm and potential spectral energy distribution are consistent with it being a luminous star-forming galaxy at high redshift. We set constraints on the orbital properties of planet b assuming coplanarity with the observed disk.

Key words: circumstellar matter – planetary systems – stars: individual (HD 95086) – submillimeter: stars

1. Introduction

Debris disks were discovered by *IRAS* (Aumann et al. 1984) as infrared excess emission from dust orbiting stars and sustained by collisions of leftover planetesimals and cometary activity. They often have a structure analogous to that of minor body belts in the solar system, with asteroid- or Kuiper-Belt components. The majority of the known debris disks are massive Kuiper-Belt analogs not only because the collisional evolution proceeds more slowly at large orbital distances, but also because stars are faint in the far-infrared, making positive identifications of excess from cold debris much easier. It is interesting to note that the first Kuiper-Belt Objects in our own solar system were not discovered until 1992 (Jewitt & Luu 1993), eight years later than the *IRAS* discovery.

Planets, minor bodies, and leftover planetesimals all form as a consequence of agglomeration processes that occur within the protoplanetary disk. Interactions between them during the formation and subsequent evolution leave signs in the disk that can be used to study the current state and past history of a planetary system. Therefore, these faint dusty disks are excellent tools to understand the outer zones of exoplanetary systems, including our own.

Through sensitive infrared surveys, hundreds of debris disks are known (Matthews et al. 2014), providing a rich resource to study planetary system evolution and architecture. Although thousands of exoplanets and candidates have been discovered through radial velocity and transit measurements, this breakthrough is currently biased toward the inner zones of systems and is not sensitive to planets like Jupiter and Saturn beyond 5 au. Recent improvements in high-contrast imaging have enabled us to find planets out at the same stellocentric distance scales as the debris disks. Fomalhaut (Kalas et al. 2008), HR 8799 (Marois et al. 2008, 2010), β Pic (Lagrange et al. 2009), HD 95086 (Rameau et al. 2013), HD 106906 (Bailey et al. 2014), and 51 Eri (Macintosh et al. 2015) are prominent examples of such systems known to host both debris disks and directly imaged planets.

From the observed dust temperatures derived from disk spectral energy distributions (SEDs) of ~200 debris disks, Ballering et al. (2013) report a weak trend that the inner edge of the cold planetesimal zone appears to depend on the luminosity/temperature of the star, indicating a signpost for planetary migration and/or shepherding. However, disk extents estimated from SEDs are degenerate. Any inferred radii depend strongly on the assumed composition and the particle size

---

[14] Current address: Department of Terrestrial Magnetism, Carnegie Institution for Science, 5241 Broad Branch Road, Washington, DC 20015, USA.

[15] Current address: Center for Exoplanets & Habitable Worlds, Pennsylvania State University, University Park, PA 16802, USA.

distribution. Because of this degeneracy, it is very difficult to directly translate SED measurements into physical sizes. Even when resolved images are available (mostly in the far-infrared), the exact location of the parent bodies is still uncertain because of the effect of non-gravitational forces (radiation and drag) on small grains. The true parent-body distribution in debris disks can be provided by resolved submillimeter/millimeter images, which probe large (millimeter-sized) grains that stay close to their parent bodies. Disk morphologies suggestive of influences from unseen planets, such as resonance clumps (Wyatt 2003) and/or apocenter glow (Pan et al. 2016), are also best observed at submillimeter/millimeter wavelengths (e.g., Ertel et al. 2012; Löhne et al. 2017). Existing ALMA data on debris disks show a large variety of Kuiper-Belt analogs: some systems have very narrow rings of parent bodies (e.g., Fomalhaut; Boley et al. 2012; MacGregor et al. 2017; and ϵ Eri; Booth et al. 2017), and some have either multiple rings (HD 107146, Ricci et al. 2015a) or broad disks (HR 8799, Booth et al. 2016; τ Ceti, MacGregor et al. 2016a; 61 Vir, Marino et al. 2017). The parent-body distributions therefore give insights into the possible overall structure of the planetary systems.

HD 95086 is a young (17 ± 4 Myr; Meshkat et al. 2013) A8 star that possesses a large infrared excess, indicative of a massive debris disk (Chen et al. 2012), and a $\sim$5 M_J planet at the projected distance of $\sim$56 au (Rameau et al. 2013, 2016). Compared to the *Hipparcos* catalog, the *Gaia* DR1 catalog gives a slightly closer distance, 83.8 ± 1.9 pc (Gaia Collaboration et al. 2016), which we adopt throughout the paper. Its disk was marginally resolved by *Herschel* and found to be inclined at $\sim$25° from face-on (Moór et al. 2013). Analysis of its detailed infrared SED and reanalysis of the resolved images suggest that the debris structure around HD 95086 is very similar to that of HR 8799: a warm ($\sim$170 K) belt, a cold ($\sim$60 K) disk, and an extended disk halo (up to $\sim$800 au) (Su et al. 2015). Modeling the disk surface brightness distribution at 70 and 160 μm suggests that the extended emission seen in the far-infrared is largely from the small grains produced by frequent collisions due to dynamical stirring of planetesimals and launched from the system by stellar radiation in the form of a disk halo. Therefore, the inclination derived from the *Herschel* images might not be a true representative of the planetesimal disk or be subject to a large error. It is then crucial to measure the intrinsic distribution of the planetesimal population as traced by millimeter emission from large grains in order to properly characterize the possible perturbers, HD 95086 b and any unseen planet(s) interior to the cold disk.

Here we present the first millimeter observations of the HD 95086 system, obtained by the Atacama Large Millimeter/submillimeter Array (ALMA). Our observations reveal the location of the cold Kuiper-Belt analog for the first time. The paper is organized as follows. Details about the observations and general data reduction are given in Section 2. In Section 3 we first present the dust continuum map of the system, which can be described as an inclined ring plus a bright point source near the outer edge of the ring. We then determine the properties of the disk (flux and geometry) and those of the bright source (flux and position) using both visibilities and imaging model approaches. In Section 4 we revise the disk SED based on the new observations, discuss the ring's width and possible asymmetry and the likely nature of the bright source, and obtain new constraints on HD 95086 b. Conclusions are given in Section 5.

2. Observations

We observed HD 95086 with ALMA in Band 6 (1.3 mm) under two projects: 2013.1.00773.S, PI: Su (referred to as data set A) and 2013.1.00612.S, PI: Booth (referred to as data set B). The observations consist of 12 single-pointing block executions centered at HD 95086 (phase center R.A.: 10:57:02.91 decl.: −68:40:02.27 (J2000)). The majority of the observations were obtained in 2015 April/May, while one was made in 2015 January. The proper motion of the star (pmra = -41.11 ± 0.03 mas yr^{-1} and pmdec = 12.91 ± 0.03 mas yr^{-1}) gives 11 mas offset for the three-month time span, i.e., there is no significant pointing difference in these observations. Table 1 lists the details about these observations including dates, block id, number of antennas used, projected baselines, weather conditions, on-source integration time, and flux calibrators.

The correlator setup was designed to optimize the continuum sensitivity, but also covered the ^{12}CO J = 2-1 transition at 230.538 GHz with 3840 channels over a bandwidth of 1.875 GHz. The setup was slightly different between the two projects. The four basebands were centered at 215, 217, 230, and 232.5 GHz for data set A, but at 231.87, 232.55, 245, and 247 GHz for data set B. The raw data were processed by the ALMA Regional Centers using the CASA package (ver. 4.2.2 for data set A and ver. 4.3.1 for data set B). Nearby quasars and solar system objects (Callisto and Ganymede) were used for flux calibration, resulting in an absolute flux uncertainty $\lesssim$10% (the Technical Handbook for cycle 2). The total on-source integration time is 4.58 hr for data set A, and 4.54 hr for data set B. No CO detection was reported in the pipeline reduced product. Details regarding the CO gas in the system will be reported in another publication (M. Booth et al. 2017, in preparation).

3. Results and Analysis

3.1. Continuum Emission

We generated the calibrated measurement sets using the scripts provided by the ALMA project for each of the data sets. We then split the observations into different fields (pointing) and spectral windows by binning the time sampling to 30 s and averaging the spectral channels with a width of 128 channels. These averaged, binned *uv* visibilities were then exported to FITS format for further analysis using the MIRIAD software (Sault et al. 1995). Visibilities were then inverted with natural weighting, deconvolved, and restored to generate a final synthesized map using the standard procedures in MIRIAD.

For data set A, the synthesized continuum image is shown in Figure 1(a) with a synthesized beam of $1''.28 \times 1''.03$ and a position angle (P.A., measured from north toward east) of 75°.1, and an rms of 8.7 μJy beam^{-1}. For data set B, the image is shown in Figure 1(b) with a synthesized beam of $1''.20 \times 1''.04$ and a P.A. of 79°.4, and an rms of 11.0 μJy beam^{-1}. In both images, a ring-like structure is clearly seen with a very bright point-like source offset from the star $\sim$3″ away at a P.A. of 293° (−67°). Since the quality (rms and beam) of both data sets was similar, we then combined both data sets and generated a slightly deeper continuum map (shown in Figure 1(c)). The combined continuum map has a synthesized beam of $1''.22 \times 1''.03$ and a P.A. of 77°.4, and an rms of 7.5 μJy beam^{-1}. The ring's circumference is detected at a signal-to-noise ratio (S/N) $\gtrsim$ 15σ per beam, and is slightly

Table 1
Observational Log

Date	Block UID	Number of Used Antennas	Baselines (m)	PWV (mm)	$T_{\rm sys}$ (K)	Time on Source (minutes)	Hour Angle At Midpoint	Flux Calibrator
2013.1.00773.S, Data Set A								
2015 Jan 28	X1beb	38	15.1–348.5	1.27	83.7	45.86	+02:25	J1107
2015 Apr 04	Xba2	39	15.1–327.8	1.02	73.8	45.86	−00:38	Callisto
2015 Apr 05	X267e	39	15.1–327.8	1.28	77.2	45.86	−00:09	Ganymede
2015 Apr 05	X2a9e	39	15.1–327.8	1.27	77.3	45.86	+01:27	J1107
2015 Apr 05	X2e6d	39	15.1–327.8	1.25	80.7	45.86	+02:55	Titan
2015 Apr 06	X14f2	36	15.1–327.8	1.23	76.5	45.86	+01:47	J1107
2013.1.00612.S, Data Set B								
2015 Apr 10	X1412	35	15.3–348.5	2.14	101.0	45.36	+00:14	Ganymede
2015 Apr 10	X1d34	35	15.3–348.5	2.38	108.9	45.36	+02:16	J1107
2015 Apr 14	Xbb6	36	15.3–348.5	3.65	144.6	45.36	−01:18	Ganymede
2015 Apr 23	X1462	39	15.1–348.5	1.88	103.3	45.36	+03:12	Titan
2015 May 01	X883	37	15.1–348.5	1.95	100.7	45.36	+00:55	Ganymede
2015 May 02	Xd15	37	15.1–348.5	1.18	85.0	45.36	+00:15	Ganymede

inclined from face-on. We estimate the pointing accuracy of the data, ~resolution/(S/N), to be $0\farcs13$ since the main ring is detected at $S/N \gtrsim 10$.

We adopt two approaches to explore the best-fit parameters for the HD 95086 system: (1) visibilities fitting, and (2) image-plane fitting. In both approaches, we assume that the millimeter emission can be described by an optically and geometrically thin (no scale height) model plus a point source offset from the center. We explore two simple axisymmetric models to describe the disk: (1) a two-boundary disk confined in a radial span of $R_{\rm in}$ and $R_{\rm out}$ with a surface density power law of $\Sigma(r) \propto r^p$, where r is the stellocentric distance, and (2) a Gaussian ring defined by the peak (R_p) and the width (FWHM) of the ring (R_w). For the millimeter emission of the disk (i.e., dominated by large grains), we expect that the dust temperatures follow $T_d(r) = 278.3 L_*^{0.25} r^{-0.5}$, where L_* is the stellar luminosity in units of the solar luminosity ($6\,L_\odot$ for HD 95086 using the new distance) and r is in au. The disk has a total flux, $F_{\rm tot}$, at 1.3 mm, and its midplane is assumed to incline by an angle of i from face-on (i.e., $i = 0°$), with the major axis along a position angle (P.A.). Three parameters describe the bright source: the total flux ($F_{\rm pt}$), and the offset from the star (Δx and Δy). We discuss the results in the following subsections for both approaches, and synthesize the final best-fit model parameters in Section 3.4.

3.2. Visibilities Modeling Approach

We model the visibilities for both data sets simultaneously. To minimize the free parameters, we assume no offset between the center of the disk and the star. Therefore, there are a total of eight/nine free parameters to describe the system in both axisymmetric disk models: two/three parameters for the disk density distribution ($R_{\rm in}$, $R_{\rm out}$, and p for the two-boundary disk, or R_p and R_w for the Gaussian ring), two parameters for the disk viewing geometry (i and P.A.), the total flux of the disk ($F_{\rm tot}$), and three parameters for the point source (Δx, Δy and the total flux $F_{\rm pt}$). We determine the best-fit values for these free parameters independently by adopting the Markov chain Monte Carlo (MCMC) approach outlined in MacGregor et al. (2013). For all parameters, we assume uniform priors and require that the model be physically plausible (flux greater than zero and the outer radius larger than the inner one).

The best-fit parameters and their $\pm 1\sigma$ uncertainties are given in Table 2. For each set of the best-fit parameters, we generated a high-resolution model image and transformed it to the visibility domain according to the observation. We then constructed the residual map by subtracting the model from the data in the visibility domain and imaging the residual using the same procedures in MIRIAD. The residual maps are shown in Figure 2. Overall, the residuals are within $\pm 3\sigma$ for the main disk. The subtraction of the bright source is not perfect and creates an oversubtraction at the center of the bright source and positive residuals in the area around it, suggesting the source might be extended. In all residual maps, there appears to be another faint ($S/N \sim 9$) source $\sim 2\farcs5$ south of the bright one. The two axisymmetric models yield very similar parameters in terms of the disk flux, viewing geometry, and point-source parameters. However, the residual in the main disk is slightly smaller in the Gaussian-ring model. Although the residuals in the main disk tend to be more negative in the east side of the disk, the bright source is unfortunately along the west side of the major axis, making it difficult to assess any asymmetric structure present in the disk (more detail is given in Section 4.2).

3.3. Imaging Plane Modeling Approach

Given the good S/N detection of the main disk, we also try to derive the best-fit parameters for the two models by fitting in the image plane. Details about this approach can be found in Booth et al. (2016). We use the combined synthesized map for the MCMC search. For experiments, two more free parameters are included in this part of the fitting. For both models, the center of the ring is not fixed at the star position. Although a small offset[16] is preferred for both models, these values are within one pixel of the reconstructed maps ($0\farcs2$ per pixel) and within 2σ of the pointing accuracy ($\sigma \sim 0\farcs13$), therefore not significant. The final best-fit parameters and the residual maps are also given in Table 2 and Figure 2. Overall, the best-fit parameters agree with those derived from the visibilities method within the uncertainties, except for the total fluxes of the ring and the point source where the derived flux using the

---

[16] $0\farcs16$ and $0\farcs06$ for the two-boundary model, and $0\farcs21$ and $0\farcs08$ for the Gaussian ring.

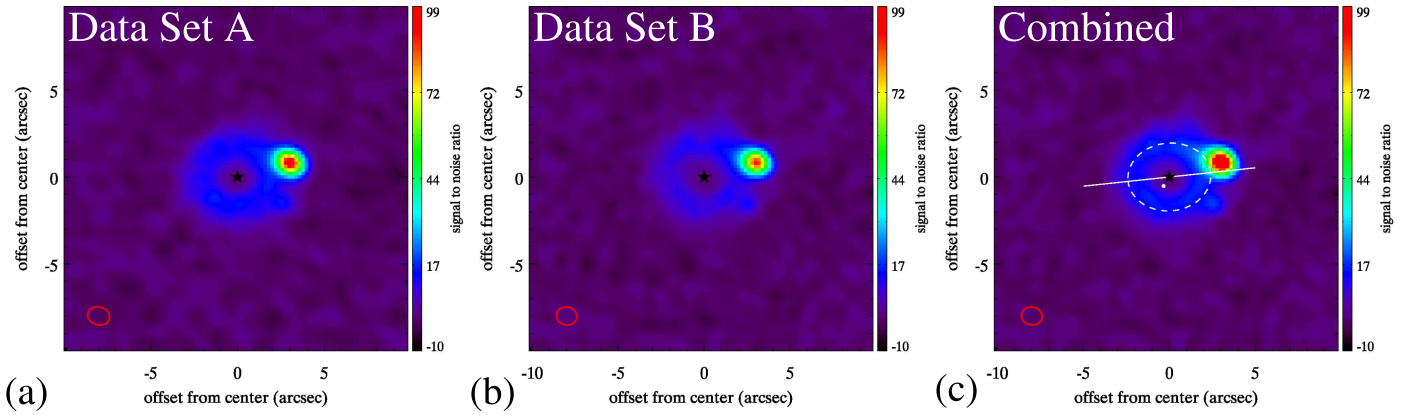

Figure 1. ALMA 1.3 mm continuum maps of the HD 95086 system. Panels (a) and (b) are the data obtained under program 2013.1.00773.S (PI: Su), referred to as data set A, and program 2013.1.00612.S (PI: Booth), referred to as data set B; (c) is the combined map using both data sets. Details about the synthesized beams (shown as the red ellipse in each of the panels) and rms of the maps are given in Section 3.1. In panel (c) we also mark the positions of the star and its planet b (as in 2016) as the black star symbol and white dot, respectively. The ring's circumference (the dashed ellipse in panel (c)) is clearly detected at $S/N \gtrsim 15$ per beam. The bright source, detected at S/N of 100, is almost aligned with the ring's major axis (white line). Its nature is discussed in Section 4.3.

imaging approach is consistently larger. We also note that the estimated uncertainties are also smaller using the image-plane approach. This is because the MCMC uncertainty depends strongly on the weightings of the data. The noise within the beam is highly correlated, and the image deconvolution (the "CLEAN" procedure) treats noise nonlinearly, both resulting in smaller uncertainties for the MCMC image fitting that might not be statistically robust. A factor equivalent to the square root of the beam size in pixels is included to mitigate the correlated noise, but this is only an approximation as it assumes a Gaussian beam, whereas the dirty beam has some low-level, non-Gaussian structure that this factor cannot account for. Fitting in the image domain is computationally faster and can achieve the same result in terms of geometric parameters for high S/N data; however, we caution against relying on the robustness of the uncertainties using imaging plane fitting.

3.4. Best-fit Disk Parameters by Minimizing Other Contamination

Since ALMA is sampling the sky with many different baselines (i.e., spatial scales) through interferometry, we can better assess the properties of the bright source by generating a map with only the long-baseline data ($>80\ k\lambda = 3\farcs1$) where any extended structure with sizes $>3\farcs1$ (i.e., the disk emission) is filtered out. The long-baseline map is shown in Figure 3(a). Within $3\farcs5$ radius from the star, there are two sources (detected above 8σ) that appear in the long-baseline map. The measured FWHM of the faint source is $0\farcs79 \times 0\farcs64$, the same as the synthesized beam in the long-baseline map, while the FWHM of the bright source is ~8% broader, $0\farcs85 \times 0\farcs70$. To evaluate whether the threshold defining the long-baseline data affects the FWHM of the bright source, we also generated the long-baseline maps with different thresholds between 60 and 80 $k\lambda$. The FWHM of the bright source is consistently broader than the synthesized beam by 8%. Furthermore, we generated individual long-baseline maps per data set to see whether a flux difference exists between the two data sets for the bright source. Taken at face value, the bright source is about 5% brighter in data set B. Given the typical absolute flux uncertainty (10%) in the ALMA data, the flux difference is not significant. The properties (offset and flux density) of the two point sources are determined using "uvmodelfit" in CASA, and given in Table 3. The flux of the bright source in the long-baseline data is 9% lower than the flux derived by simultaneously fitting the disk and point source.

We then generated a "disk-only" map by subtracting the best-fit point sources in the visibility domain. The disk-only map is shown in Figure 3(b). The subtraction of the bright source is far from perfect. There is still significant flux ($\gtrsim 25\sigma$) near the east side of the bright source, which could be part of the disk structure; alternatively, it might mean that the bright source has a non-symmetric, extended shape. If the bright source is a dusty galaxy in nature (see Section 4.3), it is very likely to have an irregular shape, making it challenging to separate it from the disk without high angular resolution observations. The subtraction of the faint source is better. The emission near the position of the faint source is more smooth, but it does appear that the disk flux extends toward the faint source, explaining the residual in Figure 2. Similarly, the observed resolution prevents further assessment.

To evaluate the impact of the two sources on the derived disk parameters, we searched for the best-fit disk parameters using the visibility approach by fixing the properties of the two point sources. The best-fit disk parameters are basically the same as those without fixing the two point sources (Section 3.2). The residual maps are shown in Figures 4(a) and (b). Compared to Figures 2(a) and (b), the fits with the fixed point-source properties have no oversubtraction at the position of the bright source, but the residual around the bright source is higher.

We performed similar searches using the image-plane approach by masking out the pixels that have fluxes >0.1 mJy beam^{-1} (the region around the bright source and the center of the faint one). To explore whether allowing a slight offset between the star and the disk center can improve the results, we also allow offsets in the MCMC parameters. The best-fit disk parameters are given in Table 4. Interestingly, the disk size parameters are slightly smaller than those derived in Section 3.3, but still within the uncertainties. The residual maps are shown in Figures 4(c) and (d). The derived disk fluxes are also lower, reducing the oversubtraction in the east side of the disk. The presence of the bright source undoubtedly affects the derived disk parameters. Unfortunately, there is no easy way to mask out the contribution of the bright source in the visibility domain since the bright source contributes to all baselines. We tried to minimize the impact of the bright source by fitting it as

Table 2
MCMC Derived Disk Parameters with One Point-like Bright Source

Parameter[a]	Description	Two-boundary Disk				Gaussian Ring			
		Visibilities Modeling		Dirty Map Modeling		Visibilities Modeling		Dirty Map Modeling	
		Value	$\pm1\sigma$	Value	$\pm1\sigma$	Value	$\pm1\sigma$	Value	$\pm1\sigma$
$R_{\rm in}$ (au)	inner belt radius	107	+6 −5	110	+3 −4	⋯	⋯	⋯	⋯
$R_{\rm out}$ (au)	outer belt radius	327	+6 −7	328	+7 −6	⋯	⋯	⋯	⋯
p	surface density index	−0.48	+0.34 −0.38	−0.42	+0.13 −0.12	⋯	⋯	⋯	⋯
R_p (au)	peak radius	⋯	⋯	⋯	⋯	204	+7 −7	208	+4 −3
R_w (au)	width (FWHM)	⋯	⋯	⋯	⋯	176	+6 −6	179	+6 −6
$F_{\rm tot}$ (mJy)	total belt flux density	2.87	+0.10 −0.11	2.89	+0.08 −0.08	2.91	+0.10 −0.18	3.07	+0.09 −0.09
$F_{\rm pt}$ (mJy)	flux of Pt.[b]	0.88	+0.05 −0.05	0.92	+0.01 −0.01	0.87	+0.06 −0.06	0.92	+0.01 −0.01
Δx (″)	R.A. offset of Pt.	−3.06	+0.04 −0.04	−3.07	+0.01 −0.01	−3.05	+0.05 −0.05	−3.07	+0.01 −0.01
Δy (″)	Decl. offset of Pt.	0.85	+0.05 −0.05	0.85	+0.01 −0.01	0.85	+0.05 −0.05	0.85	+0.01 −0.01
i (°)	inclination	36	+3 −2	35	+2 −2	36	+2 −2	34	+2 −2
P.A. (°)	position angle	98	+3 −3	98	+3 −3	98	+3 −4	96	+4 −3

Notes.
[a] We adopt a distance of 83.8 pc to translate the angular scale into physical scale.
[b] Pt. is the bright point-like source near the edge of the disk.

a Gaussian profile in visibilities, allowing for some sort of extension. The results are also given in Table 4. Similar to the image-plane approach, the disk size parameters are also slightly smaller than those derived in Section 3.2. The Gaussian parameters for the bright source are basically the same as the synthesized beam, but with much lower flux than in the fits derived from the long-baseline data (Table 3). The residual maps (not shown) are not better than those in Figures 4(a) and (b) or those in Figures 2(a) and (b) as a result.

We synthesized the various fitting results as follows. The disk has a total flux density of 2.79 ± 0.1 mJy at 1.3 mm and is inclined by 30° ± 3° from face-on with a P.A. of 97° ± 3°. It is interesting to note that the best-fit models (Table 4) all prefer to have the ring center east of the star by $\sim0\farcs1$. Since the star is not detected in the ALMA data, the "translated" pointing accuracy cannot confirm such an offset. The disk is very broad ($\Delta R/R \sim 0.84$) in the millimeter continuum, and its width is resolved by ∼1.7 beam widths. As a result, we cannot determine the exact disk density distribution or the offset between the star and disk center. For the two-boundary model, the disk can be described as having sharp boundaries at $R_{\rm in} = 106 \pm 5$ au and $R_{\rm out} = 320 \pm 10$ au with a surface density power index of -0.5 ± 0.3. For the Gaussian ring, the disk is peaked at $R_p = 200 \pm 6$ au with a width of $R_w = 168 \pm 7$ au. The reduced chi-squared (χ^2) is 1.20 for the two-boundary model, but 1.15 for the Gaussian-ring model with the total number of visibilities (574358) in the fitting; similar χ^2 numbers are also found using the image-plane approach. Based on the χ^2, the Gaussian-ring model gives a slightly better fit; however, the number of free parameters is different (7 versus 8), and some of the parameters are correlated.

4. Discussion

4.1. Revised Three-component SED Model

Su et al. (2015) examined the resolved disk images of HD 95086 from *Herschel* and argued, by a detailed SED analysis, that the system is likely to possess three debris structures. The three debris components are very similar to those of the HR 8799 system—(1) an inner warm emission representing the dust in an asteroid-belt analog, (2) an outer cold emission representing the dust in a Kuiper-Belt analog, and (3) an extended disk halo surrounding the aforementioned two components and composed of small grains. Since only the extended disk halo is resolved in the far-infrared, the exact boundaries of the different components are very uncertain and not well constrained by the SED model. The presence of an asteroid-belt analog is only constrained by the excess emission detected in the *Spitzer* IRS spectrum and unresolved MIPS 24 μm photometry; therefore, its location is set by the observed dust temperature (∼175 K, i.e., 7–10 au). Given the warm temperature and large distance to the system, this asteroid-belt component is not expected to be detected or resolved by the ALMA observation.

Since we now have the measured size for the cold disk ($R_{\rm in} = 106$ au and $R_{\rm out} = 320$ au compared to the old SED 63–189 au value), the three-component SED model needs revision. Furthermore, a re-reduction of the archive APEX/LABOCA 870 μm data on HD 95086 using the techniques described in Phillips (2011) finds a total flux of 19.4 ± 11.0 mJy, much lower than the flux published by Nilsson et al. (2010). The peak emission in the 870 μm map is offset by 13″ (i.e., 2/3 of the beam diameter) from the expected star position; therefore, the quoted flux is estimated as an unresolved source at the position of the star. Owing to the large offset, we consider it as a non-detection and use 33 mJy as the 3σ upper limit. We adopted this value for further SED analysis. Using similar approaches and grain parameters as in Su et al. (2015; minimum and maximum grain sizes of ∼1.8 μm and 1000 μm, and a particle size distribution in a power-law index of −3.5), a geometrically thin constant surface density disk with a radial span of 106–320 au provides a good fit to the ALMA 1.3 mm flux and maximum allowable fluxes in the far-infrared (gray squares in Figure 5). This cold-disk SED model also agrees with the observed 7 mm flux (not shown in Figure 5) obtained by Ricci et al. (2015b) within the uncertainty. Compared to the cold-component model presented in Su et al. (2015), this revised planetesimal disk model contributes much more flux shortward of 60 μm and is the dominant component (compared to the disk halo) at 20–30 μm. With a much larger cold planetesimal disk component, the inner radius of the disk halo is more distant from the star (from

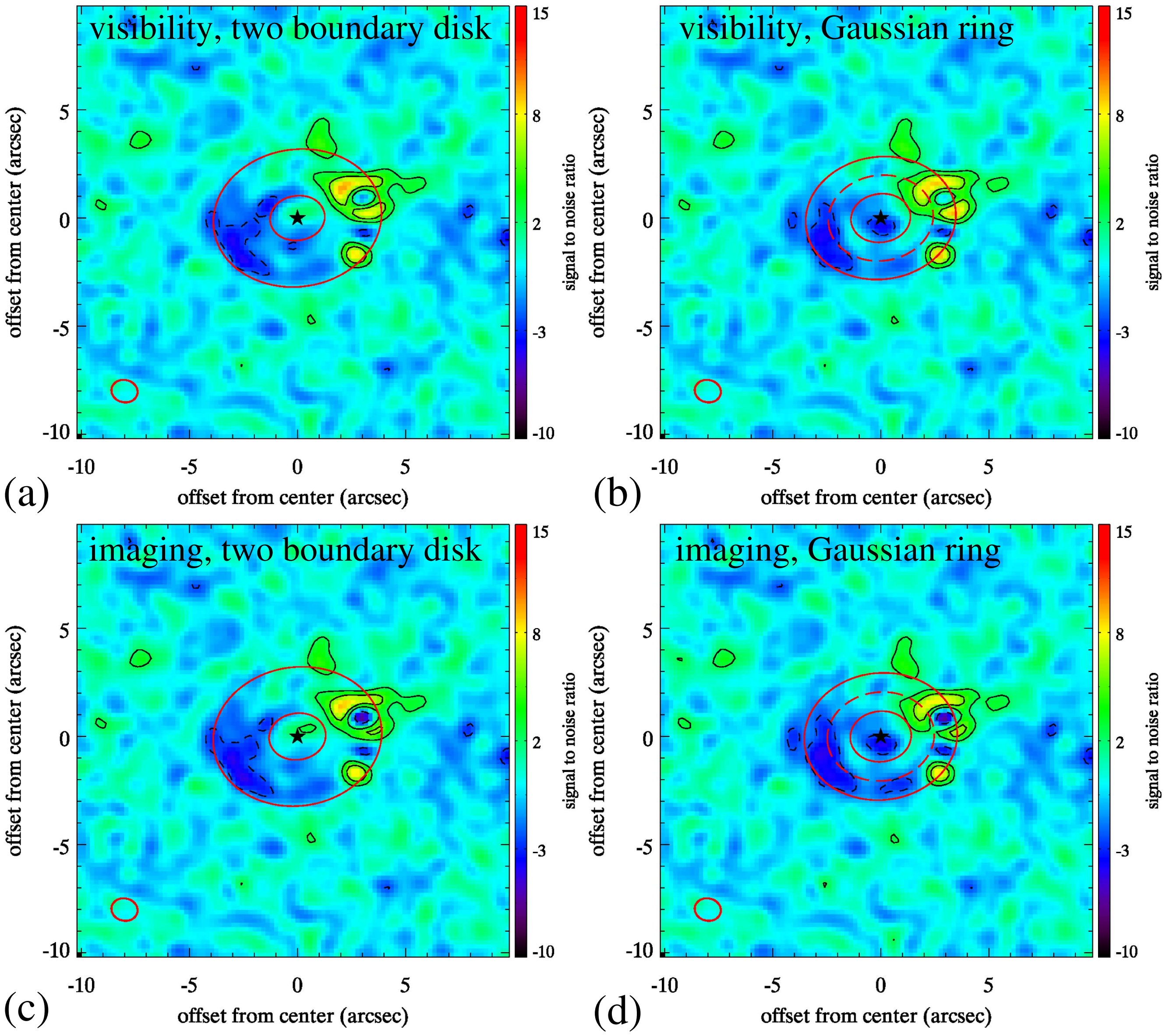

Figure 2. Residual maps of the HD 95086 system after subtracting four best-fit models (see Table 2). Panels (a) and (b) are the results using the visibilities modeling approach, while panels (c) and (d) are from the image-plane fitting. The left column is for the two-boundary disk model, where the boundaries of the disk are marked with the two red ellipses. The right column is based on the Gaussian-ring model, where the peak of the ring is marked as the red dashed ellipse, and the boundaries of the ring ($R_p \pm 0.5\,R_w$) are also shown. The display orientation (N up and E left), color scale, contours, and the star position (black star symbol) are all the same in each of the panels in units of S/N with an rms of 7.5 μJy beam^{-1}. The contour levels are in [−3, 3, 6] × rms.

old ∼190 to ∼300 au), and contributes much less flux at mid- and far-infrared wavelengths using the same grain parameters as in Su et al. (2015). Although we have now resolved the cold disk at millimeter wavelengths, revealing the placement of the large grain population, there is still a wide range of parameters that are not constrained in the SED models, especially for the grain parameters in the disk halo. The SED models shown in Figure 5 are not unique. Future resolved images of the various components at crucial mid-infrared wavelengths will shed light on this.

4.2. Ring Width and Azimuthal Asymmetry

We computed the azimuthally averaged radial profile for the disk using the synthesized image data without the two point sources (the right panel of Figure 3). Assuming the disk is inclined by 30° with the major axis along P.A. of 97°, we first created a series of elliptical rings with a width of 2 pixels (0.″4) centered at the star, and computed the average value of all pixels that fall in each ring. Since the pixels are highly correlated within the area of each synthesized beam, the noise in each ring can be approximated with the standard deviation in the ring divided by the number of beams in that ring. The background noise per ring is computed in a similar fashion. The total error in the average flux measurement per ring is therefore the nominal error and the background noise added in quadrature. The resultant disk surface brightness profile is shown in the top panel of Figure 6. For reference, the profile using the original data is also shown, and the contamination from the bright source obviously results in extra flux in the radii at 2″–4″ from the star. The point-source-subtracted ring profile is centered at $r \sim 2.''3$ from the star with symmetric profiles inside and outside the peak within uncertainties. The

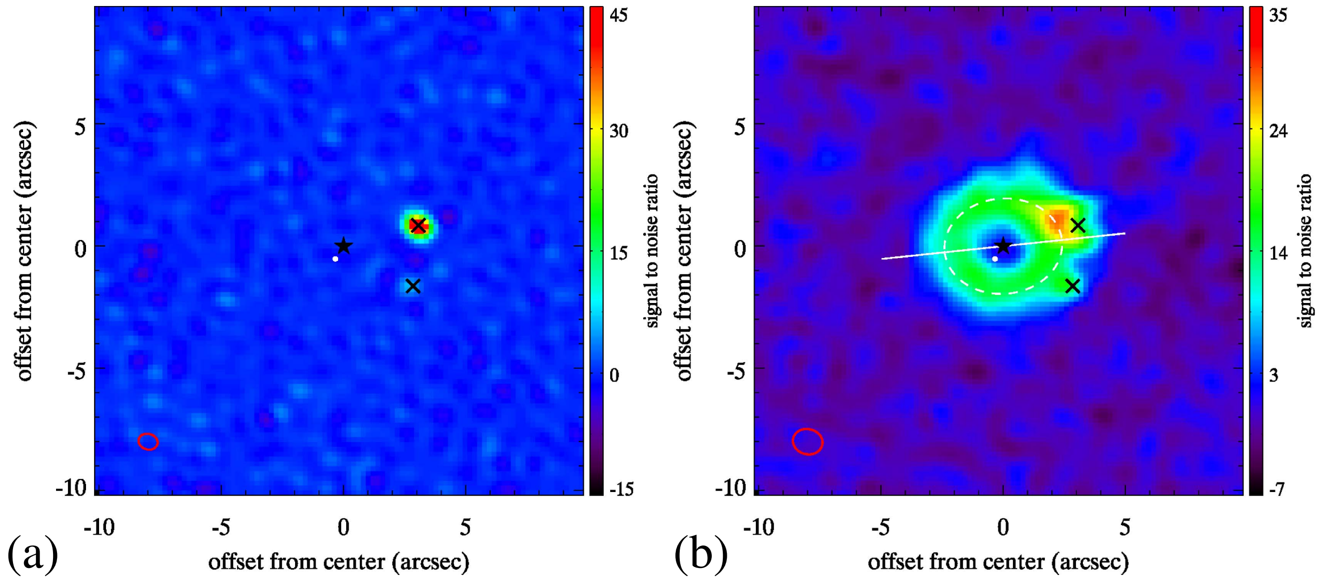

Figure 3. 1.3 mm continuum map of the point sources in panel (a) and the disk in panel (b). The left panel is generated using the long-baseline data (>80 $k\lambda$) to better illustrate the bright point-like sources (marked as black crosses). The rms in the long-baseline map is 11.4 μJy beam^{-1} and its synthesized beam is shown as the red ellipse. The right panel is the "disk-only" map generated after the subtraction of the two point sources. The positions of the star (black star symbol), planet b (white dot), and the disk major axis (white line) are also marked.

Table 3
Derived Parameters of the Two Point Sources

Parameter	Description	Point 1	Point 2
$F_{\rm pt}$ (mJy)	Flux density	0.81 ± 0.03	0.10 ± 0.02
Δx ($''$)	R.A. offset	−3.08 ± 0.04	−2.80 ± 0.03
Δy ($''$)	Decl. offset	0.83 ± 0.05	−1.61 ± 0.04

millimeter emission of the disk is surprisingly broad ($\Delta R/R \sim 0.84$).

To assess the degree of the asymmetry in the millimeter-disk emission, we also computed the radially averaged surface brightness profile along the disk circumference. To minimize the contamination of the bright source, we picked a radial span of $1\overset{''}{.}4$–$2\overset{''}{.}6$ from the star and computed the average disk brightness within an incremental angle of 27° azimuthally. Similarly, the uncertainty includes the standard deviation and background noise in each of the wedges. The azimuthal profile is shown in the bottom panel of Figure 6. The azimuthal profile agrees within 1σ to the average disk surface brightness (horizontal gray line in Figure 6), except at a P.A. of ~300°, the direction toward the bright source (although the difference is still within 2σ). Given the contamination by the bright source plus the modest resolution of the ring (~6 beam widths in circumference and $\lesssim$2 beam widths in width), the apparent asymmetry is not significant.

4.3. Possible Nature of the Bright Source

As demonstrated in Section 3.4, the bright source near the edge of the disk, at $3\overset{''}{.}2$ (a projected distance of 268 au) from the star, is slightly more extended than the synthesized beam, and roughly along the major axis of the disk (3° off). Although the disk emission can be traced up to ~320 au from the star, the peak millimeter emission is within 200 au, i.e., this bright structure is quite far away from the main location of the colliding planetesimals. We explore various possibilities for the nature of the bright source, either physically associated with the HD 95086 system or due to chance alignment of a background source.

4.3.1. Debris Phase of a Circumplanetary Disk?

It is challenging to form planets at large orbital distances through the usual route of a kilometer-sized planetesimal merger. However, there are multiple ways to bypass this hurdle, such as pebble accretion in conjunction with planet scattering (e.g., Lambrechts & Johansen 2012; Kenyon & Bromley 2015; Bromley & Kenyon 2016). Therefore, it may be possible to have a newly formed planet at ~270 au from this 17 Myr old star. Given the fact that there is no sign of this bright source in the deep K/L' data (J. Rameau 2017, private communivation) and in the mid-infrared photometry of the system (Moór et al. 2013; Su et al. 2015), it is unlikely that the bright source is the direct detection of a newly formed planet.[17] When we assume that the bright source is at the distance of 83.8 pc, the bulk of the 1.3 mm flux suggests a bolometric luminosity of 2×10^{-3} to $7 \times 10^{-5}\,L_\odot$ assuming it has a temperature of 30–100 K, which translates into a radius of 0.7–1.4 au for the optically thick emitting area. It is interesting to note that the Hill radius for a 10 $M_\oplus$ planet at 270 au around 1.6 $M_\odot$ star is ~5 au. Therefore, the millimeter flux of the bright source could come from the dust emission of a circumplanetary disk (CPD), whose typical size is expected to be one-third of the Hill radius (Martin & Lubow 2011; Zhu 2015).

The CPD is expected to be gas rich around a planet in formation, like a scaled-down version of a protoplanetary disk around a young star. With a total flux of 0.81 mJy at

---

[17] The typical temperature for a protoplanet is expected to be a few 100 to a few 1000 K (Eisner 2015; Zhu 2015).

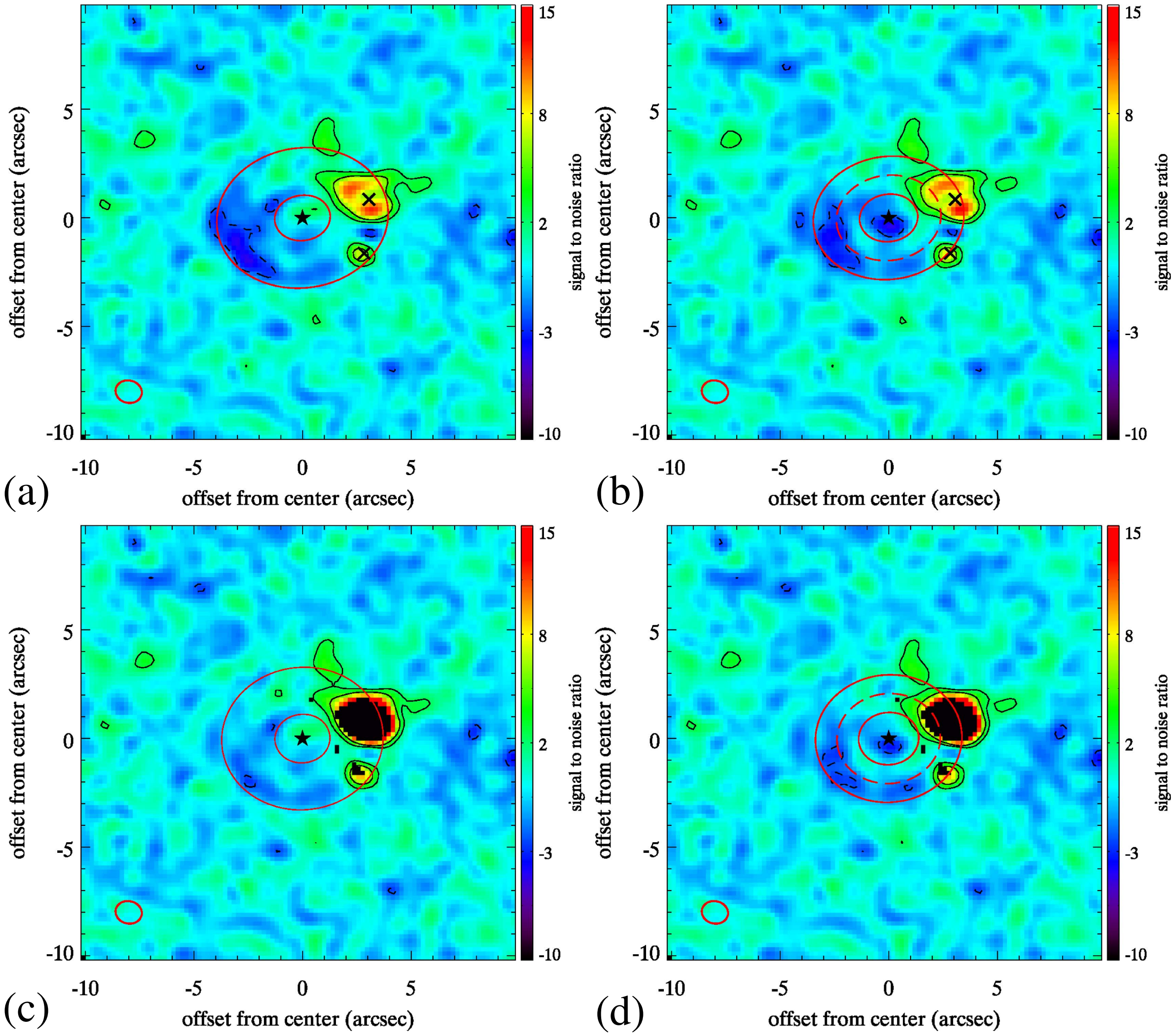

Figure 4. 1.3 mm residual maps using the best-fit parameters derived in Section 3.4 by minimizing the contamination from the bright source. Panels (a) and (b) are the residual maps for the two-boundary disk and the Gaussian ring obtained by fixing the two point-source parameters in the visibility fitting. Panels (c) and (d) are the similar residual maps using the image-plane fitting by masking pixels (black area) affected by the bright point-like sources (details see Section 3.4). The other lines, contours, and symbols are the same as in Figure 2.

1.3 mm, the estimated dust mass is ∼0.2–0.4 $M_\oplus$ assuming a typical dust opacity, $\kappa_{1.3\,\mathrm{mm}} = 2.3\,\mathrm{cm}^2\,\mathrm{g}^{-1}$ (Beckwith et al. 1990) and dust temperatures of 30–60 K. We do not detect any CO gas emission from the bright source. The noise level in the integrated CO (2-1) line flux is $1.5 \times 10^{-23}\,\mathrm{W\,m}^{-2}$ assuming a velocity dispersion of $4.6\,\mathrm{km\,s}^{-1}$ (twice the Keplerian velocity at 270 au) (M. Booth et al. 2017, in preparation). The CO gas mass for the hypothesized CPD is lower than $2.3 \times 10^{-6}\,M_\oplus$ (1σ, details see M. Booth et al. 2017, in preparation), suggesting an extremely low gas-to-dust mass ratio. If the dust emission did come from the CPD of a newly formed planet, the CPD might be in the "debris" phase as moons/satellites are being formed. However, the mass fraction between the hypothesized CPD and newly formed planet is uncomfortably high ($\sim10^{-2}$ for a Neptune-sized planet) in comparison to the typical mass fraction of 10^{-4} between the satellites and the giant planets in the solar system, making this "debris CPD" hypothesis unlikely.

4.3.2. A Dust Clump Due to a Giant Impact?

Alternatively, a recent giant impact in the disk can create a bright, concentrated region in the disk (Telesco et al. 2005). Depending on the impact velocity, the disk morphology could remain in the clump-dominated phase that lasts for a few orbital periods after a giant impact (Jackson et al. 2014). Given the system's young age, observing such a large impact at 270 au is not impossible. Next, we estimate whether the brightness/mass in the clump is consistent with such a scenario. When we use the parameters derived in Section 3.4, the bright source contributes ∼25% of the total disk flux at 1.3 mm, which is significantly larger than the clump in the β Pic disk (<4% of the disk flux).

Table 4
MCMC Derived Disk Parameters by Minimizing Other Contamination[a]

Parameter[b]	Description	Two-boundary Disk				Gaussian Ring			
		Visibilities Modeling		Dirty Map Modeling		Visibilities Modeling		Dirty Map Modeling	
		Value	$\pm1\sigma$	Value	$\pm1\sigma$	Value	$\pm1\sigma$	Value	$\pm1\sigma$
$R_{\rm in}$ (au)	inner belt radius	105	+5 −5	106	+5 −4	…	…	…	…
$R_{\rm out}$ (au)	outer belt radius	331	+4 −6	312	+7 −8	…	…	…	…
p	surface density index	−0.5	+0.3 −0.3	−0.5	+0.2 −0.2	…	…	…	…
R_p (au)	peak radius	…	…	…	…	199	+6 −6	200	+4 −4
R_w (au)	width (FWHM)	…	…	…	…	169	+5 −6	167	+7 −7
$F_{\rm tot}$ (mJy)	total belt flux density	2.77	+0.19 −0.07	2.57	+0.09 −0.08	2.72	+0.12 −0.08	2.74	+0.09 −0.10
Δx_c ($''$)	R.A. offset of ring	0.15	+0.04 −0.04	0.09	+0.03 −0.03	0.15	+0.05 −0.04	0.12	+0.04 −0.04
Δy_c ($''$)	Decl. offset of ring	0.05	+0.04 −0.04	0.05	+0.03 −0.03	0.06	+0.04 −0.04	0.08	+0.03 −0.03
i (°)	inclination	31	+3 −3	28	+3 −3	31	+2 −3	30	+3 −3
P.A. (°)	position angle	98	+4 −3	97	+6 −6	98	+4 −4	95	+5 −5

Notes.
[a] "Contamination" mainly means the bright source near the edge of the disk. In the visibility approach, a Gaussian-like profile is used to fit the bright source. In the image-plane fitting, the area affected by the bright source is masked out. Details see Section 3.4.
[b] We adopt a distance of 83.8 pc to translate the angular scale into physical scale.

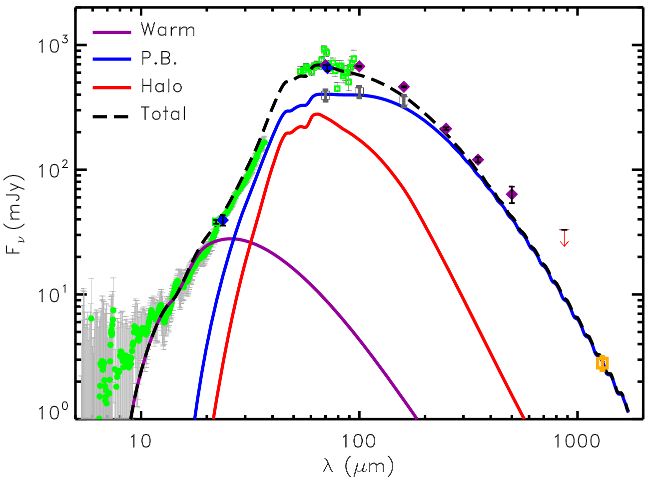

Figure 5. Revised three-component SED model of the HD 95086 system. Various symbols with error bars are measurements from Su et al. (2015). The estimated 1.3 mm disk flux from this study is shown as the orange square. Various lines are the SED models for the warm, planetesimal (P.B.), and disk halo components. The photometry points from *Herschel* (purple diamonds) and APEX are likely contaminated by the point source detected in our ALMA map, therefore, the total model disk SED (dashed line) is lower than those values. The gray squares are the maximum allowable fluxes derived from the PACS data (details see Su et al. 2015).

At 270 au, the orbital velocities are so low that most collisions between large objects would be mergers[18] and not produce much debris (with masses ∼a few % of the impactors, Jackson et al. 2014). To produce the amount of dust observed in the bright source, objects with masses $\gtrsim$10–20 $M_\oplus$ (Neptune mass) are required. Impacts involving such large objects are likely to be very explosive, i.e., the resultant clump is expected to smear and spread very rapidly after the impact (a few orbital periods). The fact that the bright source is relatively compact

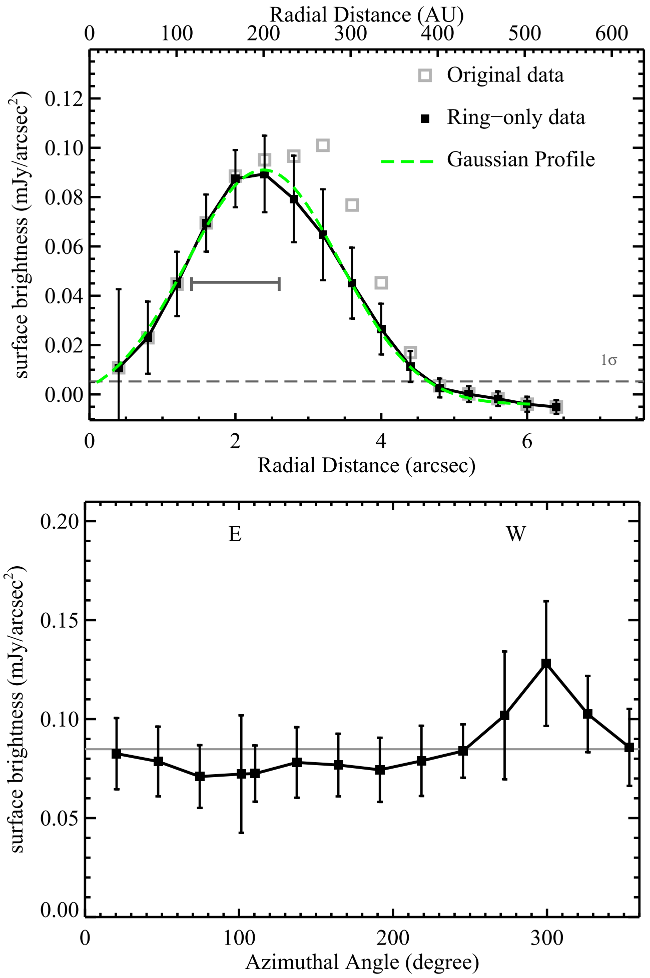

Figure 6. Top panel: azimuthally averaged radial surface brightness profile of the disk. Filled connected symbols are the profiles using the disk image after the subtraction of the two point sources, while the gray symbols are the profiles without subtraction. A best-fit, symmetric Gaussian profile is shown as the solid green line for comparison. The horizontal dashed line shows the rms of the images, and the gray bar marks the radial span that was used to compute the azimuthal angle profile. The bottom panel is the surface brightness profile of the disk along the disk circumference after the subtraction of the two point sources. The horizontal gray line represents the average disk surface brightness.

---

[18] The typical impact velocity is roughly the orbital velocity, which is ∼2.3 km s^{-1} at 270 au around HD 95086. Given the escape velocity of 25 km s^{-1} for a Neptune-like planet, a typical impact between two Neptune-like objects at 270 au belongs to the merging collision outcome based on the work by Leinhardt & Stewart (2012).

(∼8% broader than the synthesized beam in the long-baseline data) disfavors the origin of a giant impact.

4.3.3. A Dust Clump Due to Planetesimals Trapped by an Unseen Planet?

In addition, a concentrated dust clump can also be created by the intense collision among the planetesimals trapped in the resonance with an unseen planet (Wyatt 2003), as one of the proposed origins for the dust clump in the β Pic disk. The dust clump in the β Pic disk is also found to be very bright in CO gas emission, probably released by the icy planetesimals (Matrà et al. 2017). Therefore, we might also expect to detect a significant amount of CO gas associated with the bright source in HD 95086 if all the planetary systems have a similar composition. The upper limit on the integrated CO (2-1) line flux is ∼100 times fainter than the integrated line flux of CO (2-1) line in the β Pic disk after scaling by the distance difference, while the dust flux in the clump is much brighter in the HD 95086 disk. Given these comparisons, it seems unlikely that the bright source has a similar nature as the clump in the β Pic disk.

4.3.4. Alignment of a Background Galaxy

An alternative explanation is that the source is a background galaxy. In fact, Su et al. (2015) suspected that the integrated submillimeter flux of the system is likely contaminated by background galaxies because of the excess emission detected at *Herschel*/SPIRE bands and APEX 870 μm compared to the disk SED model. When we use the parameters of the Schechter function in Carniani et al. (2015), the probability of a galaxy with an 1.3 mm flux of >0.81 mJy within 4″ of the star is ∼0.5%, but increases to 5% and 14% chance within the FWHM and 10% of the primary beam, respectively. For the fainter source, the probability of having a source with an 1.3 mm flux of >0.1 mJy within 4″ of the star is 11.4%. When we assume that the two sources are physically not related, the chance of both being located within 4″ of the star is 0.06%. The contamination from multiple background point sources is also seen around ϵ Eri (Chavez-Dagostino et al. 2016). Therefore, it is possible that the sources in HD 95086 are related background galaxies, and the 0.06% probability is then a lower limit. These values are a statistical assessment given an ensemble of observations, and the application to one single observation is not a one-to-one correspondence. Based on these probabilities, the faint source is very likely a background galaxy; the bright source could be a background galaxy; this would be a rare case, but not impossible.

In general, a background galaxy might have a steep dust spectrum, like $\nu^{3.5}$, and the debris disk is likely to be shallower, like $\nu^{2.6}$ (MacGregor et al. 2016b; Holland et al. 2017). Therefore, a background galaxy is likely to be brighter in data set B than in data set A because of the frequency difference if the absolute flux calibration in both data sets is consistent. As estimated in Section 4.1, the flux difference of the bright source between the two data sets is within the uncertainty of absolute flux calibration, i.e., not significant. Alternatively, we can compare the spectral indexes between the bright source and the disk. Spectral index maps were generated with the data sets combined and separately using all baselines and long baselines alone. Figure 7 shows the spectral index map of the combined data set. The bright source has a spectral index of 3.0 ∼ 4.0 derived from the combined data. Owing to the S/N in the extended emission, the spectral index across the whole disk varies, but the index of the disk is generally shallower than the index of the bright source.

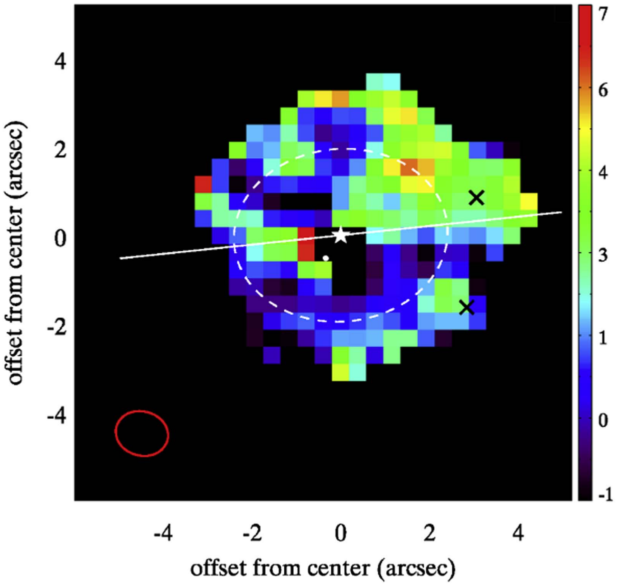

Figure 7. Spectral index map of the combined data set. To enhance the S/N in the spectral index map, a pixel of 0.″4 was used. The star, planet b, disk major axis, and the two point sources are all marked as in previous figures.

A steeper spectral index does not necessarily mean that the bright source is indeed a background galaxy because an impact-produced clump may also have a steep particle size distribution, resulting in a high spectral index. When we assume that this is indeed the case, the spectral slope suggests that the clump should have a total flux of a few hundred mJy at 200 μm from extrapolating the measured flux of 0.81 mJy at 1.3 mm. The flux of such a clump at 70–100 μm range would have been even brighter, i.e., comparable to the total disk flux in the far-infrared. Given the measured disk SED (Figure 5), it would be very difficult for such a component to coexist with other components (planetesimal disk and disk halo), which corroborates our early assessment.

As a sanity check, we can also construct the SED of the bright source using the measured 1.3 mm flux and the revised three-component disk SED presented in Section 4.2. By comparing the photometric measurements and the model disk SED, the “excess” emission, presumably from the bright source, is 31.4 ± 18.9 mJy, 30.9 ± 10.6 mJy, 24.8 ± 10.4 mJy, and 10.1 ± 11.0 mJy at 250, 350, 500, and 870 μm, respectively (the quoted errors include 10% uncertainty from the SED model). With the 1.3 mm flux measured by ALMA, the SED of the bright source is shown in Figure 8, and the SED is consistent with that of a dusty star-forming galaxy at $z = 2$ (Casey et al. 2014). The angular size of the bright source (Section 3.4) is in the range of angular sizes for luminous infrared and submillimeter galaxies at $z \sim 2$ measured in the radio (Gurvits et al. 1999; Rujopakarn et al. 2016). It seems very plausible that this bright source is the result of the chance alignment of a background galaxy.

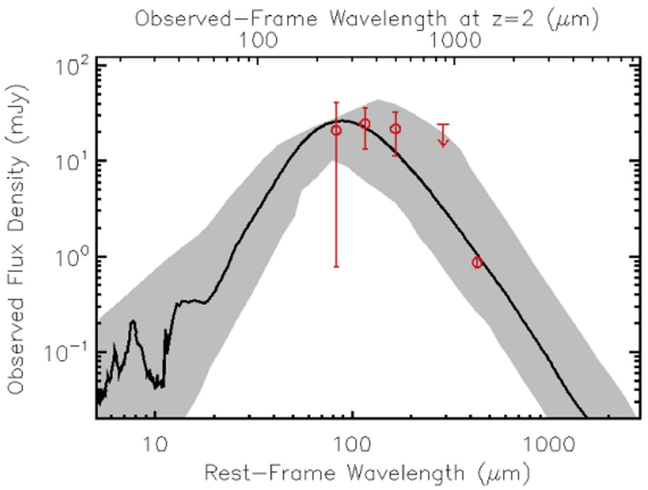

Figure 8. Possible SED of the background galaxy at 250, 350, and 500 μm (SPIRE bands) and at 1.3 mm. The flux density in the SPIRE bands is estimated by the excess emission between the observed values and the SED model, and the 1.3 mm flux density is directly measured from the ALMA data. The black line shows a representative SED for a submillimeter galaxy from Pope et al. (2008), and the gray area shows the plausible range of background galaxies of fixed infrared luminosity $10^{12.5}\,L_\odot$ (adopted from Casey et al. 2014.)

4.4. Constraints for the HD 95086 b from the Disk Perspective

HD 95086 b was discovered by Rameau et al. (2013) at an angular separation of 0.″60–0.″63 from the star (Rameau et al. 2016). At a distance of 83.8 pc, this translates into a projected distance of 50.3–52.3 au. When we assume that planet b and the disk are coplanar, the inclination of the disk (30° ± 3°) implies that planet b has a stellocentric distance of 56–63 au (∼semimajor distance if planet b is on a circular orbit). The bright source makes it difficult to assess the asymmetry in the disk, and no "significant" asymmetry is present in the millimeter-disk emission. Alternatively, we can also place some constraint on the eccentricity of the shepherding planet orbit, presumably planet b, by determining the offset of the ring and the star (i.e., the offset is ∼ae, where a is the semimajor distance and e is the eccentricity). As discussed earlier, we did not detect a significant offset between the ring center and the star. The expected pointing accuracy, ∼resolution/(S/N), is 0.″13 since the main ring is detected at S/N $\gtrsim$ 10. The non-detection of an offset suggests $e < 0.17$ for the shepherding planet (presumably planet b) with a semimajor distance of 63 au.

The most recent orbital parameters for HD 95086 b are from Rameau et al. (2016), where a small angular movement is detected using the data obtained by Gemini/GPI between 2013 and 2016: a semimajor distnce of $61.7^{+20.7}_{-8.4}$ au, an inclination of $27°^{+10}_{-13}$, and an eccentricity lower than 0.2. With the revised distance of 83.8 pc to HD 95086, we revise the semimajor distance of HD 95086 b to $57.2^{+19.2}_{-7.8}$ au. These orbital parameters are all consistent with those derived from the disk geometry (assumed coplanar). The mass of the planet is estimated to be 4.4 ± 0.8 $M_{\rm Jup}$ (De Rosa et al. 2016). The 5σ detection limits from VLT/NaCo and Gemini/GPI observations suggest that our current high-contrast capability is not sensitive to planet masses lower than 1.5 $M_{\rm Jup}$ in the 60–800 au region from the star (Rameau et al. 2016).

When we assume that the mass of the star is 1.6 ± 0.16 $M_\odot$, the mass ratio between planet b and the star, $\mu \equiv M_p/M_*$, is (1.95–3.45) × 10^{-3}. For this mass ratio, the timescale to clear the planet's chaotic zone is $\lesssim$1 Myr (Morrison & Malhotra 2015), much shorter than the estimated ∼17 Myr age of the system. We adopt the numerically derived formula from Morrison & Malhotra (2015) to compute the size of the planet's chaotic zone. Assuming planet b is at a circular orbit with a semimajor axis of a_p, the interior chaotic zone width is $\Delta a_{\rm int} = 1.2\mu^{0.28}a_p$ and the exterior chaotic zone width is $\Delta a_{\rm ext} = 1.7\mu^{0.31}a_p$. With the range of μ and a_p (56–63 au), the width of the exterior chaotic zone is 14–19 au, suggesting that the outer boundary of the chaotic zone from planet b is 70–82 au. If the inner edge of the disk is at 106 au, as derived from the two-boundary model in Section 3.4, an eccentricity of $e \sim 0.29$ is needed to extend its chaotic zone to the inner edge of the disk if planet b is the shepherding planet and coplanar with the disk. This eccentricity is marginally consistent (<2σ) with no significant offset detected between the ring center and the star. If we relax the assumption that the disk and the planet are coplanar, HD 95086 b's chaotic zone can reach 98 au assuming a semimajor distance of 76 au (the maximum allowable range from high-contrast imaging; Rameau et al. 2016). A low eccentricity ($e \sim 0.08$) can extend the planet's influence to 106 au (the inner boundary of the disk). Therefore, planet b can be the shepherding planet to maintain the inner edge of the Kuiper-Belt analog. In summary, the values listed above are all within the allowable ranges for the system.

If the system hosts an additional planet outside the orbit of HD 95086 b that is shepherding the inner edge of the cold disk, it would have to be lower than 1.5 $M_{\rm Jup}$ to have eluded detection (Rameau et al. 2016). From the dynamical stability criteria of Gladman (1993) and Morrison & Kratter (2016), the estimated separation between planet b and the disk is sufficient for another planet below this mass threshold to reside there while remaining long-term dynamically stable with respect to planet b if both possess low orbital eccentricities. However, the youth of this system (∼17 Myr) and long dynamical timescales at these large orbital distances place a lower limit on planets that could have cleared debris from their chaotic zones over the system's lifetime. From the clearing timescales estimated in Morrison & Malhotra (2015), a putative low-eccentricity, coplanar outer planet orbiting in the region beyond planet b's orbit and interior to the cold disk would have to be $\gtrsim$0.2 $M_{\rm Jup}$ (∼4 Neptune masses) to have cleared debris from that region over the system's lifetime. In summary, the shepherding planet between planet b and the inner edge of the cold disk would have a mass of 0.2–1.5 $M_{\rm Jup}$ with the assumption of coplanarity and low eccentricity.

5. Conclusion

We obtained an ALMA 1.3 mm image of HD 95086, a young (∼17 Myr) star hosting a directly imaged planet and a debris disk composed of dust generated in massive asteroid- and Kuiper-Belt analogs. The high angular resolution (a beam of 1.″1) and sensitivity (rms of 7.5 μJy beam^{-1}) provided by ALMA enable us to resolve the Kuiper-Belt analog for the first time. The sensitive ALMA millimeter image reveals an inclined ring centered at the star and a bright source near the edge of the ring along the major axis of the ring. Our observations also covered the the ^{12}CO $J = $ 2-1 transition at 230.538 GHz, and no CO emission above 3σ per beam was found in the pipeline-produced CO channel maps in the region of the ring and the bright source.

To access the properties of the bright source, we also generated the continuum map using data with baselines longer than 60–80 $k\lambda$, where an extended structure like the planetesimal disk is filtered out. The long-baseline data reveal two sources within $3\farcs5$ of the star (a much fainter source south of the bright one). The FWHM of the sources is consistent with being a point source, although the bright one is slightly broader (8%) than the synthesized beam. We determined the best-fit parameters (total fluxes and positions) of the two sources in the long-baseline data using point-source fitting in the visibility domain. The faint source has a 1.3 mm flux of 0.1 mJy ($S/N \gtrsim 9$ in the long-baseline map), and is most likely a background galaxy, similar to other faint sources in the long-baseline map. The bright source is detected at high S/N with a total 1.3 mm flux of 0.81 mJy and located $-3\farcs08$ E and $0\farcs83$ N of the star. We explored the possible nature of the bright source, including (1) a debris phase of the CPD, (2) a dust clump produced by a giant impact, (3) a dust concentration due to planetesimals trapped by an unseen planet, and (4) a background dusty galaxy. The source's brightness in dust continuum and non-detection of the CO emission suggest that it is unlikely to have resulted from a structure physically assocated with the system (the first three scenarios), and more likely due to chance alignment of a background source. We further constructed the SED of the bright source using the 1.3 mm flux and the "excess" emission by comparing the unresolved photometry and the expected disk emission, and found that it is consistent with the expected SED from a $z = 2$ dusty galaxy. The slight extension of the bright source and the steeper spectral index compared to the spectral index of the disk are both consistent with the bright source being a luminous high-redshift galaxy.

We used the MCMC approach to determine the best-fit parameters of the disk. We assumed that the Kuiper-Belt analog can be described by simple parametric models. We explored two axisymmetric, geometric thin models for the disk surface density profiles: (1) a two-boundary power-law disk with sharp inner and outer boundaries, and (2) a Gaussian ring. We further assumed that the millimeter emission comes from large grains whose temperatures follow a $r^{-0.5}$ power law. The best-fit parameters and associated uncertainties are derived by fitting the visibilities and image-plane data. We found that fittings in the visibilities and image-plane domain give consistent results within $\pm1\sigma$ uncertainties in terms of the geometric parameters (disk extent, position, and inclination angles and the offset of the bright source); however, the derived fluxes are consistently higher when using the fits in the image plane. Although within the uncertainties, the flux of the bright source is also brighter than that derived from the long-baseline data, implying a difficulty of separating the disk from the bright source. We then synthesized the disk parameters by (1) fixing the point-source parameters in the visibilities fit, (2) masking out the pixels affected by the bright source in the imaging fit, and (3) fitting the bright source as a Gaussian profile. The final parameters for the Kuiper-Belt analog are all very similar. The major axis of the disk is along P.A. of $97° \pm 3°$ with the midplane inclined by $30° \pm 3°$ from face-on. The width of the disk is very broad and resolved by $\lesssim$2 beam widths. The disk density profile is consistent with either (1) a broad Gaussian ring peaked at 200 ± 6 au with a FWHM width of 168 ± 7 au, or (2) an $r^{-0.5\pm0.3}$ power-law profile with an inner radius of 106 ± 5 au and outer radius of 320 ± 10 au. Although the residual maps (data–model) are very similar between the two models, the Gaussian-ring model gives a slightly better reduced χ^2. In all residual maps, the east side of the disk has more negative residuals than the opposite side, suggesting an apparent disk asymmetry. However, the residual in the west side of the disk is also contaminated by the imperfect subtraction of the bright source. Judging from the azimuthal profile along the disk circumference, the apparent asymmetry is not significant.

We also explored whether allowing an offset between the ring and the star would produce a better residual map. Although a small offset (within $0\farcs15$, ~one-eighth of the synthesized beam) is preferred in χ^2 statistics, it produces no significant difference in the residual map. Based on the estimated pointing accuracy of $0\farcs13$, the non-detection of an offset suggests that the orbit of the shepherding planet has an eccentricity <0.17 if it has a semimajor axis of 63 au. Given the observed projected separation between HD 95086 b and the star, the semimajor axis of the orbit of planet b is 56–63 au if the planet and the disk share the same orbital plane and the planet is on a circular orbit. The estimated major axis is consistent with the apparent motion of the planet detected within three years. However, in the coplanar case for a planet on a circular orbit, the expected chaotic zone of planet b (maximum of 82 au) does not reach the inner boundary of the disk (~106 au). If planet b is the shepherding planet to maintain the inner edge of the cold disk, an eccentricity $\gtrsim$0.29 is needed to extend its influence. Such a planet would create an offset of $0\farcs2$ between the star and the ring center, which is marginally consistent with the observed data. It is also possible that planet b is not the shepherding planet for the cold disk given the large separation between its chaotic zone and the inner disk edge. An additional unseen low-mass planet (0.2–1.5 $M_{\rm Jup}$) on a circular orbit can also occupy the dust-free zone between planet b and the cold disk and may have eluded detection. Alternatively, relaxing the coplanarity assumption, a larger semimajor axis of planet b (76.4 au, still within the allowable range) and a low eccentricity (~0.08) would extend its chaotic zone to ~106 au.

We thank Alan Jackson for the discussion on the evolution of impact-produced clumps, and Benjamin Weiner for the discussion on the properties of background galaxies. We are grateful to George Rieke for his thorough proofreading of the manuscript. We also thank Julien Rameau for providing additional inforamtion about the background source, and Scott Kenyon and Ya-Lin Wu for their comments. M.B. is grateful to Bruce Sibthorpe and Andrés Jordán for the help during proposal preparation. K.Y.L.S. acknowledges the partial support from the NASA grant NNX15AI86G. M.A.M. acknowledges support from the National Science Foundation under Award No. 1701406. M.B. acknowledges support from the Deutsche Forschungsgemeinschaft (DFG) through project Kr 2164/15-1. R.M. acknowledges research support from NASA (grant NNX14AG93G) and NSF (grant AST-1312498).

This paper makes use of the following ALMA data: ADS/JAO.ALMA 2013.1.00773.S and 2013.1.00612.S. ALMA is a partnership of ESO (representing its member states), NSF (USA) and NINS (Japan), together with NRC (Canada) and NSC and ASIAA (Taiwan) and KASI (Republic of Korea), in cooperation with the Republic of Chile. The Joint ALMA Observatory is operated by ESO, AUI/NRAO and NAOJ. The National Radio Astronomy Observatory is a facility of the

National Science Foundation operated under cooperative agreement by Associated Universities, Inc.

This work has made use of data from the European Space Agency (ESA) mission *Gaia* (http://www.cosmos.esa.int/gaia), processed by the *Gaia* Data Processing and Analysis Consortium (DPAC, http://www.cosmos.esa.int/web/gaia/dpac/consortium). Funding for the DPAC has been provided by national institutions, in particular the institutions participating in the *Gaia* Multilateral Agreement.

Facility: Atacama Large Millimeter/submillimeter Array (ALMA).

ORCID iDs

Kate Y. L. Su https://orcid.org/0000-0002-3532-5580
Meredith A. MacGregor https://orcid.org/0000-0001-7891-8143
Mark Booth https://orcid.org/0000-0001-8568-6336
David J. Wilner https://orcid.org/0000-0003-1526-7587
Kevin Flaherty https://orcid.org/0000-0003-2657-1314
Renu Malhotra https://orcid.org/0000-0002-1226-3305
Antonio S. Hales https://orcid.org/0000-0001-5073-2849
Sarah Morrison https://orcid.org/0000-0002-2432-833X
Brenda C. Matthews https://orcid.org/0000-0003-3017-9577
Simon Casassus https://orcid.org/0000-0002-0433-9840

References

Aumann, H. H., Beichman, C. A., Gillett, F. C., et al. 1984, ApJL, 278, L23
Bailey, V., Meshkat, T., Reiter, M., et al. 2014, ApJL, 780, L4
Ballering, N. P., Rieke, G. H., Su, K. Y. L., & Montiel, E. 2013, ApJ, 775, 55
Beckwith, S. V. W., Sargent, A. I., Chini, R. S., & Guesten, R. 1990, AJ, 99, 924
Boley, A. C., Payne, M. J., Corder, S., et al. 2012, ApJL, 750, LL21
Booth, M., Dent, W. R. F., Jordán, A., et al. 2017, MNRAS, 469, 3200
Booth, M., Jordán, A., Casassus, S., et al. 2016, MNRAS, 460, L10
Bromley, B. C., & Kenyon, S. J. 2016, ApJ, 826, 64
Carniani, S., Maiolino, R., De Zotti, G., et al. 2015, A&A, 584, A78
Casey, C. M., Narayanan, D., & Cooray, A. 2014, PhR, 541, 45
Chavez-Dagostino, M., Bertone, E., Cruz-Saenz de Miera, F., et al. 2016, MNRAS, 462, 2285
Chen, C. H., Pecaut, M., Mamajek, E. E., Su, K. Y. L., & Bitner, M. 2012, ApJ, 756, 133
De Rosa, R. J., Rameau, J., Patience, J., et al. 2016, ApJ, 824, 121
Dent, W. R. F., Wyatt, M. C., Roberge, A., et al. 2014, Sci, 343, 1490
Eisner, J. A. 2015, ApJL, 803, L4
Ertel, S., Wolf, S., & Rodmann, J. 2012, A&A, 544, A61
Gaia Collaboration, Prusti, T., de Bruijne, J. H. J., et al. 2016, A&A, 595, A1
Gladman, B. 1993, Icar, 106, 247
Gurvits, L. I., Kellermann, K. I., & Frey, S. 1999, A&A, 342, 378
Holland, W. S., Matthews, B. C., Kennedy, G. M., et al. 2017, arXiv:1706.01218
Jackson, A. P., Wyatt, M. C., Bonsor, A., & Veras, D. 2014, MNRAS, 440, 3757
Jewitt, D., & Luu, J. 1993, Natur, 362, 730
Kalas, P., Graham, J. R., Chiang, E., et al. 2008, Sci, 322, 1345
Kenyon, S. J., & Bromley, B. C. 2015, ApJ, 806, 42
Lagrange, A.-M., Gratadour, D., Chauvin, G., et al. 2009, A&A, 493, L21
Lambrechts, M., & Johansen, A. 2012, A&A, 544, A32
Leinhardt, Z. M., & Stewart, S. T. 2012, ApJ, 745, 79
Löhne, T., Krivov, A. V., Kirchschlager, F., Sende, J. A., & Wolf, S. 2017, A&A, in press, arXiv:1704.08085
MacGregor, M. A., Lawler, S. M., Wilner, D. J., et al. 2016a, ApJ, 828, 113
MacGregor, M. A., Matrà, L., Kalas, P., et al. 2017, ApJ, 842, 8
MacGregor, M. A., Wilner, D. J., Chandler, C., et al. 2016b, ApJ, 823, 79
MacGregor, M. A., Wilner, D. J., Rosenfeld, K. A., et al. 2013, ApJL, 762, L21
Macintosh, B., Graham, J. R., Barman, T., et al. 2015, Sci, 350, 64
Marino, S., Wyatt, M. C., Kennedy, G. M., et al. 2017, MNRAS, 469, 3518
Marois, C., Macintosh, B., Barman, T., et al. 2008, Sci, 322, 1348
Marois, C., Zuckerman, B., Konopacky, Q. M., Macintosh, B., & Barman, T. 2010, Natur, 468, 1080
Martin, R. G., & Lubow, S. H. 2011, MNRAS, 413, 1447
Matrà, L., Dent, W. R. F., Wyatt, M. C., et al. 2017, MNRAS, 464, 1415
Matthews, B. C., Krivov, A. V., Wyatt, M. C., Bryden, G., & Eiroa, C. 2014, in Protostars and Planets VI, ed. H. Beuther et al. (Tucson, AZ: Univ. Arizona Press), 521
Meshkat, T., Bailey, V., Rameau, J., et al. 2013, ApJL, 775, L40
Moór, A., Ábrahám, P., Kóspál, Á, et al. 2013, ApJL, 775, L51
Morrison, S., & Malhotra, R. 2015, ApJ, 799, 41
Morrison, S. J., & Kratter, K. M. 2016, ApJ, 823, 118
Nilsson, R., Liseau, R., Brandeker, A., et al. 2010, A&A, 518, A40
Pan, M., Nesvold, E. R., & Kuchner, M. J. 2016, ApJ, 832, 81
Phillips, N. M. 2011, PhD thesis, Univ. Edinburgh
Pope, A., Chary, R.-R., Alexander, D. M., et al. 2008, ApJ, 675, 1171
Rameau, J., Chauvin, G., Lagrange, A.-M., et al. 2013, ApJL, 772, L15
Rameau, J., Nielsen, E. L., De Rosa, R. J., et al. 2016, ApJL, 822, L29
Ricci, L., Carpenter, J. M., Fu, B., et al. 2015a, ApJ, 798, 124
Ricci, L., Maddison, S. T., Wilner, D., et al. 2015b, ApJ, 813, 138
Rujopakarn, W., Dunlop, J. S., Rieke, G. H., et al. 2016, ApJ, 833, 12
Sault, R. J., Teuben, P. J., & Wright, M. C. H. 1995, in ASP Conf. Ser. 77, Astronomical Data Analysis Software and Systems, ed. R. A. Shaw, H. E. Payne, & J. J. E. Hayes (San Francisco, CA: ASP), 433
Su, K. Y. L., Morrison, S., Malhotra, R., et al. 2015, ApJ, 799, 146
Su, K. Y. L., & Rieke, G. H. 2014, in IAU Symp. 299, Exploring the Formation and Evolution of Planetary Systems (Cambridge: Cambridge Univ. Press), 318
Su, K. Y. L., Rieke, G. H., Malhotra, R., et al. 2013, ApJ, 763, 118
Su, K. Y. L., Rieke, G. H., Stapelfeldt, K. R., et al. 2009, ApJ, 705, 314
Telesco, C. M., Fisher, R. S., Wyatt, M. C., et al. 2005, Natur, 433, 133
Wyatt, M. C. 2003, ApJ, 598, 1321
Zhu, Z. 2015, ApJ, 799, 16